Relationship between structural parameters and the Néel temperature in $Sr_{1-x}Ca_xMnO_3$ ($0 \leqslant x \leqslant 1$) and $Sr_{1-y}Ba_yMnO_3$ ($y \leqslant 0.2$)

O. Chmaissem,[1,2] B. Dabrowski,[1,2] S. Kolesnik,[1] J. Mais,[1] D. E. Brown,[1,2] R. Kruk,[1] P. Prior,[1] B. Pyles,[1] and J. D. Jorgensen[2]
[1]*Department of Physics, Northern Illinois University, DeKalb, Illinois 60115*
[2]*Materials Science Division, Argonne National Laboratory, Argonne, Illinois 60439*
(Received 10 April 2001; published 11 September 2001)

The crystal and magnetic structures of newly synthesized $Sr_{1-x}Ca_xMnO_3$ ($0 \leqslant x \leqslant 1$) and $Sr_{1-y}Ba_yMnO_3$ ($y \leqslant 0.2$) perovskite materials (of the ABO_3 type) were investigated using neutron and synchrotron x-ray powder diffraction at temperatures between 10 and 530 K. Upon decreasing the size of the *A*-site ion (or the unit-cell size) a series of structural transitions appears at room temperature from cubic $Pm\bar{3}m$ to tetragonal $I4/mcm$ (at $x \sim 0.3$) to orthorhombic *Pbnm* at $x \sim 0.4$. In agreement with neutron-diffraction data, resistive and magnetic measurements show that the samples are antiferromagnetic with Néel temperatures T_N, varying from 233 to ~125 K and from 233 to 212 K by increasing the Ca and Ba contents, respectively. The observed variation of T_N cannot be solely explained by the changes of the unit-cell size or the average Mn-O-Mn bond angle θ. The behavior of T_N can be satisfactorily described as a function of $\langle \cos^2 \theta \rangle$ related to the superexchange interaction integral, and σ^2, the *A*-site ionic size variance [L. M. Rodriguez-Martinez and J. P. Attfield, Phys. Rev. B 54, R15 622 (1996)] regardless of the structural symmetry of the perovskite material.

DOI: 10.1103/PhysRevB.64.134412 PACS number(s): 75.25.+z, 61.12.−q, 75.30.−m

I. INTRODUCTION

Colossal magnetoresistance (CMR) in perovskite manganites resulting from competing magnetic properties and charge and orbital ordering has been a fascinating subject that attracted considerable research efforts in the past few years. Several chemical combinations were synthesized of which the $La_{1-x}Sr_xMnO_3$ and $La_{1-x}Ca_xMnO_3$ systems have been studied most extensively[1,2] showing a strong correlation between ionic sizes and magnetic and structural transition temperatures.[3] In these systems, materials are usually synthesized under ambient conditions up to a limiting substitution level at the *A*-site beyond which the chemical solubility is severely limited mainly because of the decreasing average size of the Mn^{3+x} ion and the unfavorable tolerance factor of the desired phase. However, with modified synthesis routines solubility limits in some systems were recently extended up to the end members of the phase diagram, for example, $La_{1-x}Sr_xMnO_3$ ($x \geqslant 0.6$) [Ref. 4] and $Pr_{1-x}Sr_xMnO_3$ ($x \geqslant 0.5$).[5,6]

In a study to determine the size effect of the *A* site on the antiferromagnetic transition temperature T_N, MacChesney *et al.*[7] have prepared and examined $Ca_{1-z}Sr_zMnO_3$ samples (ABO_3 type) with $0 \leqslant z \leqslant 0.25$ and found that T_N increases unexpectedly with increasing the size of the unit cell. MacChesney *et al.*'s results are clearly in contradiction with predictions based on the Néel molecular-field theory of antiferromagnetism that infers that enlargement of the unit-cell size should result in decreasing the Néel temperature. These results prompted Goodenough[8] to suggest that the Néel temperature increases, for localized-electron antiferromagnetic systems such as $Ca_{1-z}Sr_zMnO_3$, because of a competition between the covalent mixing of the *B*-cation *d* orbitals of t_{2g} symmetry and the covalent mixing of the *A*-site cations with the anion *p* orbitals, thereby reducing the *B*-O-*B* interaction. The increase of T_N with increased Sr content would be therefore due to Sr being less covalent than Ca and, hence, competing less with the *B*-O-*B* interaction. Using the model of superexchange interaction, Treves, Eibschütz, and Coppens[9] and Boekema, Van Der Woude, and Sawatzky[10] showed that in rare-earth orthoferrites the change in T_N relates primarily to departures from 180° of the *B*-O-*B* interaction angle and that T_N and $\cos^2 \theta$ (where θ is the *B*-O-*B* bond angle) are linearly related. A similar dependence between the ferromagnetic transition temperature T_C and $\cos^2 \theta$ was seen in manganese-based orthorhombic materials.[11,12] Recent studies by Rodriguez-Martinez and Attfield[13] and Attfield, Kharlanov, and McAllister[14] have shown that in CMR manganese systems with constant doping level, the ferromagnetic transition temperature T_C is mainly affected by the average size of the *A*-site cations, $\langle r_A \rangle (= \Sigma y_i r_i)$, and by the *A*-site cation size variance σ^2 $(= \Sigma y_i r_i^2 - \langle r_A \rangle^2$, where r_i is the ionic size[15] and y_i is the fractional occupancy of atoms occupying the *A* site).

In order to investigate the relationship between T_N and structural parameters (e.g., Mn-O-Mn bond angle, σ^2, $\langle r_A \rangle$) in orthorhombic, tetragonal, and cubic materials, we synthesized a series of metastable $Sr_{1-x}Ca_xMnO_3$ ($0 \leqslant x \leqslant 1$) and $Sr_{1-y}Ba_yMnO_3$ ($y \leqslant 0.2$) perovskites in which the nominal Mn oxidation state is always 4+. Insofar as we are aware, samples from the $Sr_{1-x}Ca_xMnO_3$ series with strontium content greater than 0.5 (except the end member $SrMnO_3$),[16] and the Ba-substituted materials have not been previously synthesized and little is known about their structural behavior and properties. Poepplemeier *et al.*,[17] using x ray and neutron diffraction, determined the room-temperature crystal structures for stoichiometric $CaMnO_3$ and oxygen deficient $CaMnO_{2.5}$ to be orthorhombic *Pnma* and orthorhombic *Pbam* (with a $2a_p \times 4a_p \times 1a_p$ superstructure), respectively. $CaMnO_{3-\delta}$ was shown by MacChesney *et al.*[7] and by Zeng, Greenblatt, and Croft[18] to be antiferromagnetic (T_N of ~123–125 K) of the *G* type with a weak ferromagnetic com-

ponent that was explained as possibly due to the anisotropy imposed by orthorhombic distortion. Briático *et al.*,[19] however, showed that this ferromagnetic component saturates at $\sim 0.04\mu_B$ for stoichiometric $CaMnO_3$ (in agreement with Jonker's results[20]) and decreases to about $0.01\mu_B$ with decreased oxygen content for $CaMnO_{2.84}$.

In this paper, we report the physical properties and evolution of the structure of $Sr_{1-x}Ca_xMnO_3$ ($0 \leqslant x \leqslant 1$) and $Sr_{1-y}Ba_yMnO_3$ ($y \leqslant 0.2$) investigated by neutron and synchrotron x-ray powder diffraction. With the continuous decrease of the average size of the *A* site, we observe a series of room-temperature structural-phase transitions from cubic $Pm\bar{3}m$ ($x \leqslant 0.2$, $y \leqslant 0.2$) to tetragonal $I4/mcm$ ($0.3 \leqslant x \leqslant 0.4$) to orthorhombic *Pbnm* ($0.5 \leqslant x \leqslant 1.0$). Neutron-diffraction data and resistive and magnetic measurements show that the samples are antiferromagnetic with Néel temperatures T_N varying from 233 to $\sim$125 K and from 233 to 212 K by increasing the Ca (x up to 1.0) and Ba ($y \leqslant 0.2$) contents, respectively. We demonstrate that the observed variation of T_N cannot be solely explained by the changes of the unit-cell size or by the Mn-O-Mn bond angle. T_N can be better described in terms of $\langle \cos^2 \theta \rangle$ and the variance σ^2 of sizes of the *A*-site ions.

II. SAMPLE PREPARATION AND EXPERIMENTAL DETAILS

Polycrystalline $Sr_{1-x}Ca_xMnO_3$ ($0 \leqslant x \leqslant 1$) and $Sr_{1-y}Ba_yMnO_3$ ($y \leqslant 0.2$; Δx and Δy intervals of 0.1) samples were synthesized from stoichiometric mixtures of $CaCO_3$, $SrCO_3$, $BaCO_3$, and MnO_2. The $0.6 \leqslant x \leqslant 1.0$ samples were processed using the standard solid-state reaction method and fired in air several times at various temperatures up to 1350 °C followed by slow cooling to 500 °C. The remaining compositions ($0 \leqslant x \leqslant 0.5$) and $y \leqslant 0.2$ were synthesized using a two-step method previously developed for similar metastable compounds.[21] In the first step, single-phase oxygen-deficient perovskites were obtained from precursors fired in flowing argon (containing ~ 10 ppm O_2 or less) at temperatures increasing from 1150 °C for $x = 0.5$ ($Sr_{0.5}Ca_{0.5}MnO_{2.68}$) to 1400 °C for $x = 0$ ($SrMnO_{2.61}$). In the second step, oxygen-deficient samples were annealed in air at 500 °C to bring the oxygen content up to 3.00 ± 0.01 oxygen atoms per formula unit (stoichiometry monitored using thermogravimetric analysis). All samples were phase pure according to x-ray and neutron powder diffraction. Details of the synthesis procedure, thermogravimetric measurements, structural, magnetic, and resistive properties for the oxygen deficient materials will be published separately.[22]

Magnetization and resistivity measurements were performed using a quantum design physical properties measurement system—model 6000 at temperatures between 10 and 350 K. Synchrotron x-ray diffraction data were collected on the BESSRC-CAT beam line at the advanced photon source using an intense x-ray beam of wavelength 0.7749 Å. Samples were placed in glass capillaries and measured at temperatures between 18 and 350 K using a closed-cycle helium refrigerator. Time-of-flight neutron powder diffraction data were collected on the special environment powder diffractometer[23] at the intense pulsed neutron source. Diffraction data were acquired at room temperature and for some selected samples at temperatures between 10 and 530 K using a closed-cycle helium refrigerator with heating capabilities. High-resolution backscattering data, from 0.5 to 4 Å, were analyzed using the Rietveld method and the general structure analysis system code (GSAS). [24]

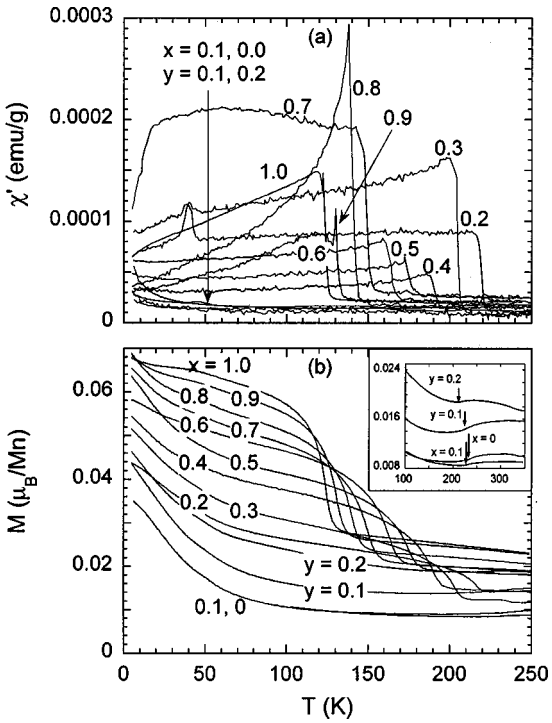

FIG. 1. Temperature dependences of (a) ac susceptibility and (b) "Field-cooled" dc magnetization for $Sr_{1-x}Ca_xMnO_3$ and $Sr_{1-y}Ba_yMnO_3$.

III. MAGNETIC AND RESISTIVE PROPERTIES

The temperature dependence of ac susceptibility in zero-magnetic field of $Sr_{1-x}Ca_xMnO_3$ and $Sr_{1-y}Ba_yMnO_3$ samples is presented in Fig. 1(a). For $0.2 \leqslant x \leqslant 1.0$, we observe a sharp step in ac susceptibility on decreasing temperature followed by a slow decrease at lower temperatures. The "field-cooled" magnetization measured on cooling in a magnetic field of 5 T is presented in Fig. 1(b). Below the kink at the paramagnetic-antiferromagnetic transition the magnetization increases to a value of $0.07\mu_B$/Mn at low temperatures with x increasing to 1.0. This indicates weak ferromagnetic behavior of $Sr_{1-x}Ca_xMnO_3$ possibly of the Dzyaloshinsky-Morya type since the $x = 0.3-1$ compounds show structural distortions from the cubic structure. We define the Néel temperature T_N as the temperature of the maximum slope in the ac susceptibility or dc magnetization vs temperature curves. Both ac susceptibility and magnetization measurements give the same values of T_N. The inset to Fig. 1(b) shows a different behavior of the magnetization for the cubic $x = 0,0.1$ and $y = 0.1,0.2$ samples. The magnetization decreases at T_N and then starts to increase at much lower temperatures. For these samples, T_N values were determined more precisely

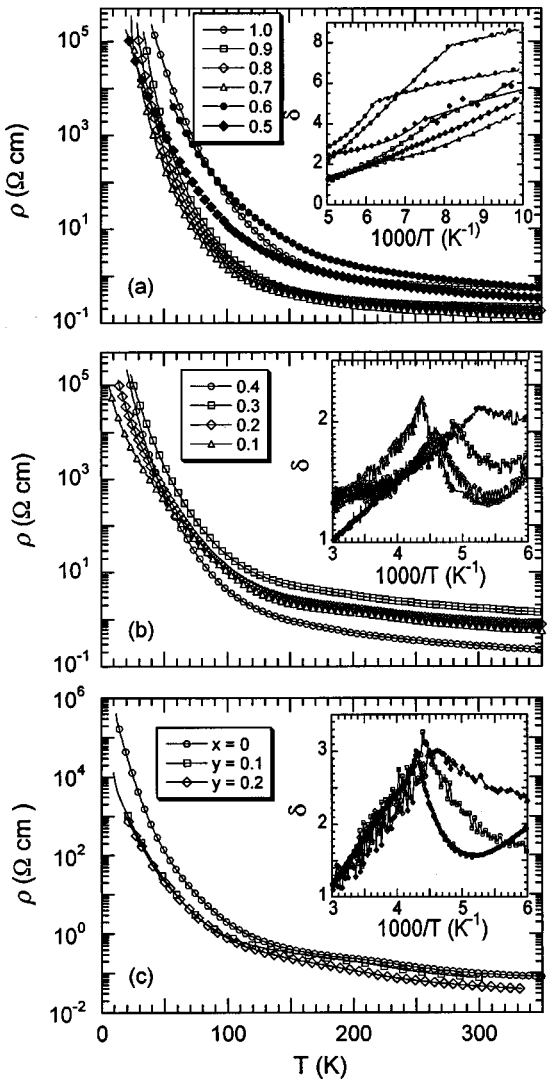

FIG. 2. Resistivity measurements for $Sr_{1-x}Ca_xMnO_3$ and $Sr_{1-y}Ba_yMnO_3$ as a function of temperature. Insets show the logarithmic derivative $\delta = d \ln \rho / d \ln(1/T)$ as a function of the inverse temperature.

from the derivatives of the resistivity measurements as described in the paragraph below and shown in the insets of Figs. 2(b) and 2(c). The arrows in the inset to Fig. 1(b) show the values of $T_N = 233$ K for $x = 0$, 228 K for $x = 0.1$, and 225 K for $y = 0.1$.

The temperature dependence of resistivity of $Sr_{1-x}Ca_xMnO_3$ and $Sr_{1-y}Ba_yMnO_3$ samples is presented in Fig. 2. Because we find that the measured resistivity is independent of the magnetic field up to the value of 7 T, we present here the data obtained in zero field. The logarithmic derivative of the resistivity[25] $\delta = d \ln \rho / d \ln(1/T) = [p(E/kT)^p] - s$ (where $p = 1$ for thermally activated conduction, E is the activation energy, and $s = 1/2$ from Mott[26]) plotted as a function of inverse temperature (see insets) is roughly linear above and below T_N for $x \geqslant 0.4$ and shows a change of the slope at a temperature that corresponds to the magnetically determined T_N. Our observation points to a significant change of the activation energy E at the antiferromagnetic transition. For example, for $CaMnO_3$ E changes from ~40 meV in the antiferromagnetic state to ~160 meV in the paramagnetic state, and for $Sr_{0.4}Ca_{0.6}MnO_3$ the corresponding change for E is 35 to 140 meV. These values are comparable to an average $E \sim 89$ meV for $CaMnO_3$, which was attributed to thermal activation of charge carriers from impurity states to the extended states in the conduction band.[27] For higher Sr content ($x \leqslant 0.4$), δ shows a sharp cusp at T_N and a complicated behavior of resistivity below T_N.

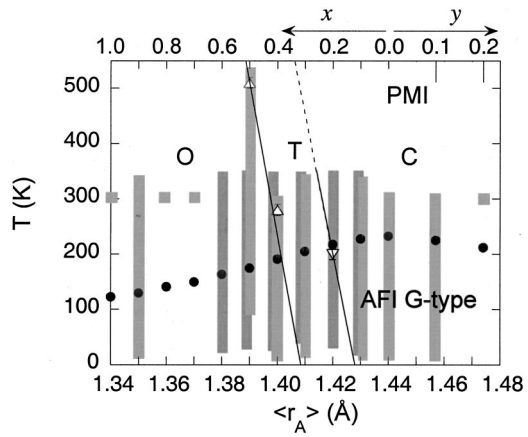

FIG. 3. Structural and magnetic phase diagram of $Sr_{1-x}Ca_xMnO_3$ and $Sr_{1-y}Ba_yMnO_3$ showing cubic $Pm\bar{3}m$, tetragonal $I4/mcm$, and orthorhombic $Pbnm$ structural ranges as a function of $\langle r_A \rangle$. Open symbols denote structural transitions, filled circles denote measured T_Ns. Diffraction data were collected at temperature ranges shown as light shaded (neutrons) and dark shaded (synchrotron x rays) vertical bars.

The magnetic and structural phase diagrams of $Sr_{1-x}Ca_xMnO_3$ and $Sr_{1-y}Ba_yMnO_3$ are plotted in Fig. 3. For this plot and the remainder of this paper we use the T_N values determined from magnetic and resistive measurements. Despite the good agreement between these values and those obtained from the Rietveld analysis of the neutron-diffraction patterns, we shall use the more accurate magnetic and resistive T_N values measured with fine ΔT steps (< 1 K) compared to a ΔT of 10–20 K for the neutron diffraction patterns. As shown in Fig. 3, T_N increases from 123 K for $CaMnO_3$ to a maximum of 233 K for $SrMnO_3$ and then decreases for the Ba-substituted samples. While the increase of T_N for Ca-substituted samples agrees with MacChesney *et al.*'s results[7] the decrease of T_N for the Ba-substituted samples appears to be consistent with the behavior predicted from the Néel molecular-field theory of antiferromagnetism but neither can explain the observed T_N's over all structural regions.

A. Neutron and synchrotron x-ray powder diffraction

The structural phase diagram of $Sr_{1-x}Ca_xMnO_3$ and $Sr_{1-y}Ba_yMnO_3$ plotted in Fig. 3 shows the evolution of the structure as a function of $\langle r_A \rangle$ and temperature. To calculate $\langle r_A \rangle$ we used the ionic radii[15] for 12-coordinated Ca (1.34 Å), Sr (1.44 Å), and Ba (1.61 Å). As shown in the figure, the structure changes from cubic $Pm\bar{3}m$ ($x \leqslant 0.2$; $y \leqslant 0.2$) to te-

TABLE I. Room temperature structural parameters for $Sr_{1-x}Ca_xMnO_3$ and $Sr_{1-y}Ba_yMnO_3$.

	Orthorhombic *Pbnm*					Tetragonal *I*4/*mcm*			Cubic *Pm*3*m*				
	A=Ca											*A*=Ba	
x,*y*	1.0	0.9	0.8	0.7	0.6	0.5	0.4	0.3	0.2	0.1	0	0.1	0.2
a (Å)	5.265 90(8)	5.2836(1)	5.3005(2)	5.3145(1)	5.3292(2)	5.3435(1)	5.336 40(2)	5.347 10(2)	3.79 193(2)	3.798 22(1)	3.805 40(1)	3.818 34(1)	3.831 26(3)
b (Å)	5.277 90(8)	5.2862(1)	5.2945(2)	5.3031(1)	5.3140(2)	5.3272(1)							
c (Å)	7.4534(1)	7.4747(1)	7.4942(3)	7.5085(2)	7.5236(5)	7.5372(2)	7.575 00(7)	7.583 52(5)					
V (Å^3)[a]	207.152(2)	208.772(2)	210.312(3)	211.626(3)	213.076(6)	214.559(4)	215.726(4)	216.823(3)	218.093(3)	219.180(4)	220.426(4)	222.680(4)	224.948(4)
x (Sr, A)	−0.0059(5)	−0.0048(5)	−0.0019(10)	−0.0031(7)	−0.0029(15)	−0.0000(8)	0	0	0.5	0.5	0.5	0.5	0.5
y (Sr, A)	0.4667(2)	0.4721(2)	0.4769(4)	0.4815(3)	0.4865(9)	0.4911(6)	0.5	0.5	0.5	0.5	0.5	0.5	0.5
U_{iso} (Sr, A) (Å^2)[b]	0.75(2)	0.77(2)	0.80(3)	0.76(2)	0.73(4)	0.70(2)	0.69(2)	0.66(1)	0.69(1)	0.66(1)	0.60(2)	0.60(1)	0.64(3)
U_{iso}Mn (Å^2)	0.23(1)	0.26(1)	0.26(2)	0.30(2)	0.29(4)	0.31(2)	0.38(2)	0.34(2)	0.32(2)	0.34(2)	0.28(2)	0.25(1)	1.01(4)
x (O1)	−0.0653(4)	−0.0607(5)	−0.0570(9)	−0.0516(6)	−0.0480(12)	−0.0415(6)	0	0	0	0	0	0	0
y (O1)	−0.0102(2)	−0.0081(3)	−0.0076(5)	−0.0058(4)	−0.0049(12)	−0.0017(8)	0	0	0	0	0	0	0
U_{11} (O1) (Å^2)	0.65(7)	0.9(1)	0.8(2)	1.0(1)	1.0(2)	1.3(1)	1.75(7)	1.54(6)	1.5(1)	1.12(2)	0.87(3)	0.85(2)	0.98(4)
U_{22} (O1) (Å^2)	0.72(7)	0.89(9)	1.0(2)	1.2(1)	1.5(3)	1.3(2)	1.75(7)	1.54(6)	1.5(1)	1.12(2)	0.87(3)	0.85(2)	0.98(4)
U_{33} (O1) (Å^2)	0.43(6)	0.38(6)	0.4(1)	0.30(9)	0.2(2)	0.2(1)	0.73(9)	0.25(7)	0.7(1)	0.44(3)	0.37(5)	0.35(3)	0.54(7)
U_{12} (O1) (Å^2)	0.07(4)	0.18(5)	0.14(9)	0.19(7)	−0.0(2)	0.4(1)	0	0					
x (O2)	0.2128(2)	0.2158(3)	0.2198(5)	0.2227(3)	0.2271(6)	0.2325(3)	0.2265(1)	0.2314(1)					
y (O2)	0.2866(2)	0.2846(2)	0.2818(4)	0.2784(2)	0.2744(5)	0.2687(3)	0.2735(1)	0.2686(1)					
z (O2)	0.0337(2)	0.0315(2)	0.0286(4)	0.0265(3)	0.0235(6)	0.0211(3)	0	0					
U_{11} (O2) (Å^2)	0.52(3)	0.56(4)	0.70(7)	0.81(5)	0.9(1)	0.95(8)	0.55(2)	0.79(2)					
U_{22} (O2) (Å^2)	0.37(3)	0.45(4)	0.41(6)	0.52(4)	0.5(1)	0.62(7)	0.55(2)	0.79(2)					
U_{33} (O2) (Å^2)	0.73(3)	0.84(4)	1.13(8)	1.09(6)	1.2(2)	1.33(9)	2.49(8)	1.60(7)					
U_{12} (O2) (Å^2)	−0.23(3)	−0.31(3)	−0.32(5)	−0.41(4)	−0.41(1)	−0.45(7)	−0.40(4)	−0.36(4)					
U_{33} (O2) (Å^2)	0.10(4)	−0.00(5)	−0.11(9)	−0.15(6)	0.0(1)	−0.20(8)	0	0					
U_{23} (O2) (Å^2)	−0.09(3)	−0.13(4)	−0.00(8)	−0.06(5)	0.2(1)	0.2(1)	−0.04(7)	0	0				
R_{wp}%[c]	6.23	6.09	7.50	6.37	8.15	5.82	8.69	7.37	8.17	8.33	4.35	8.16	11.19
χ^2	1.80	2.07	1.31	1.61	1.19	1.47	1.76	1.62	1.87	1.66	1.72	1.94	1.36
Mn-O1-Mn (°)	158.83	160.34	161.52	163.27	164.40	166.58	180	180	180	180	180	180	180
Mn-O2-Mn (°)	157.39	158.88	160.85	162.53	164.80	167.33	169.26	171.49	180	180	180	180	180
$\langle\cos^2\theta\rangle$	0.857 99	0.875 72	0.894 77	0.912 30	0.930 07	0.949 97	0.976 85	0.985 40	1	1	1	1	1
σ^2 (Å^2)	0	0.0009	0.0016	0.0021	0.0024	0.0025	0.0024	0.0021	0.0016	0.0009	0	0.0026	0.00462
obs.T_N(K)	123	130	141	150	164	175	191	205	218	228	233	225	212
Calc.T_N(K)	123.65	132.80	143.97	154.97	167.15	181.98	203.17	211.26	225.00	228.50	233.00	220.00	209.88

[a] V multiplied by four for samples with the cubic structure.
[b] U_{iso}=isotropic thermal factor.
[c] R_{wp}=weighted profile residual agreement factor.

tragonal *I*4/*mcm* ($0.3 \leqslant x \leqslant 0.4$) to orthorhombic *Pbnm* ($0.5 \leqslant x \leqslant 1.0$) forming regions that are separated by steep-phase boundary lines.

A similar sequence of structural phase transitions was previously observed for $Sr_{1-x}Ca_xTiO_3$ [Refs. 28,29] and $Sr_{1-x}Ca_xVO_3$.[30] In $Sr_{1-x}Ca_xTiO_3$, Ball *et al.*[28] suggested, based on the examination of observed x-ray superlattice reflections and the corresponding TiO_6 octahedral tilts, that a second orthorhombic *Bmmb* phase exists in a narrow region (for *x* near 0.5) between the orthorhombic *Pbnm* phase and the tetragonal *I*4/*mcm* phase. Later, x-ray diffraction studies carried out by Qin *et al.*[29] reported that the *Bmmb* phase in the $Sr_{1-x}Ca_xTiO_3$ series is possible but could not be confirmed in a definitive way, thus, leaving this question open. $Sr_{1-x}Ca_xVO_3$ was not reported to exhibit such an intermediate phase. In our present study, both the *Pbnm* and *Bmmb* structural models were examined for $x=0.4$ and 0.5. Good fits were obtained using the *Pbnm* model while the *Bmmb* model resulted in unstable refinements and poor fits. Table I lists the structural parameters for $Sr_{1-x}Ca_xMnO_3$ ($0 \leqslant x \leqslant 1$) and $Sr_{1-y}Ba_yMnO_3$ ($y \leqslant 0.2$).

1. The cubic structure

The large average ionic size of the *A* site in $Sr_{1-x}Ca_xMnO_3$ ($x \leqslant 0.2$) and $Sr_{1-y}Ba_yMnO_3$ ($y \leqslant 0.2$) results in a simple cubic structure with lattice dimensions comparable to those of the primitive perovskite (a_p). The structure can be simply described as a three-dimensional stacking of corner-sharing MnO_6 regular octahedra formed by six equivalent Mn-O bonds. Sr, Ca (or Ba) atoms occupy the cavities formed between the MnO_6 octahedra and are coordinated with 12 first-neighboring oxygen atoms. Figure

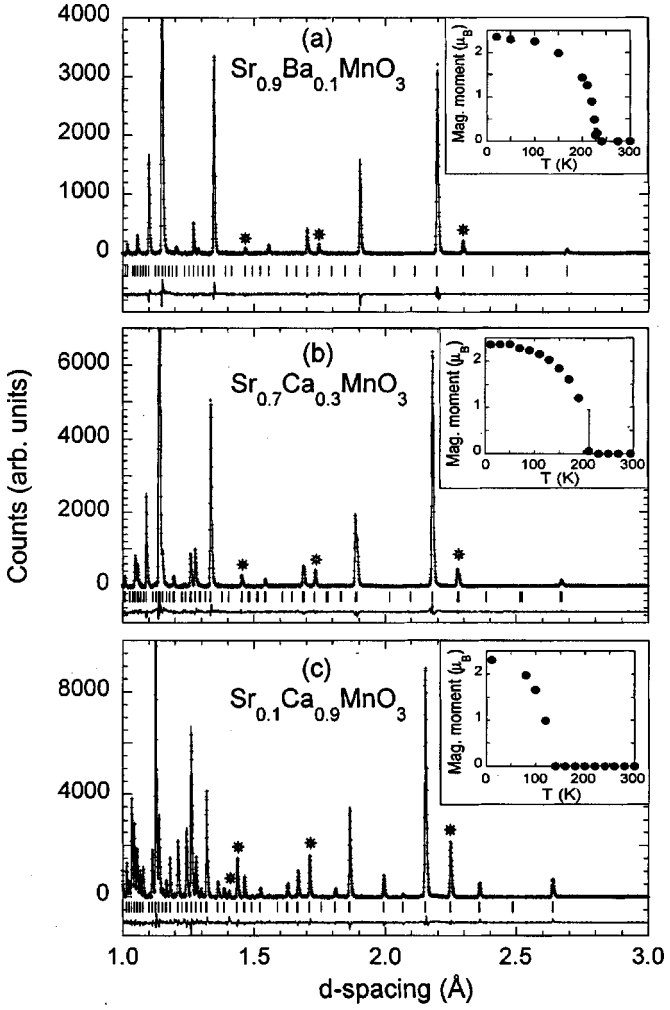

FIG. 4. Best-fit Rietveld refinement using neutron powder diffraction data at 10 K for $Sr_{0.9}Ba_{0.1}MnO_3$ (a) $Sr_{0.7}Ca_{0.3}MnO_3$ (b) and $Sr_{0.1}Ca_{0.9}MnO_3$ (c). Magnetic intensities observed at locations marked with asterisks. The insets show the refined Mn magnetic moment for each sample.

4(a) shows the best-fit Rietveld refinement for $Sr_{0.9}Ba_{0.1}MnO_3$ using neutron-diffraction data collected at 10 K. Figure 5 shows the continuous temperature dependence of the lattice parameters for $Sr_{1-x}Ca_xMnO_3$ ($x=0,0.1$) and $Sr_{0.9}Ba_{0.1}MnO_3$ with weak changes of slope that correspond to the onset of the antiferromagnetic ordering. The antiferromagnetic structure of $Sr_{1-x}Ca_xMnO_3$ ($x \leqslant 0.2$) and $Sr_{1-y}Ba_yMnO_3$ ($y \leqslant 0.2$) is of the *G* type in which neighboring Mn moments are oriented antiparallel to each other in all three directions, thus giving rise to a magnetic structure with lattice dimensions of $2a_p \times 2a_p \times 2a_p$. The refined Mn magnetic moment for $Sr_{0.9}Ba_{0.1}MnO_3$ between 300 and 10 K is shown in the inset of Fig. 4(a).

2. The tetragonal structure

As the amount of Ca at the *A* site increases, a cubic-to-tetragonal structural phase transition develops and is clearly seen below ~200 K for $x=0.2$. Figure 6 shows synchrotron x-ray data (for $x=0.2$) taken at 50 and 350 K demonstrating

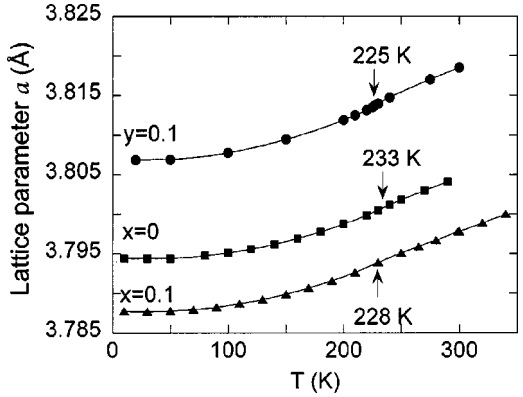

FIG. 5. Lattice parameters of cubic $Sr_{1-x}Ca_xMnO_3$ ($x=0,0.1$) and $Sr_{0.9}Ba_{0.1}MnO_3$ as a function of temperature. Weak changes of slope (denoted by the arrows) correspond to the onset of antiferromagnetic ordering.

the tetragonal splitting of several peaks at different positions. Figure 4(b) shows the best-fit Rietveld refinement for $Sr_{0.7}Ca_{0.3}MnO_3$ using the 10 K neutron diffraction data. In the tetragonal structure, the long-range structural distortions result in elongation and rotation of the MnO_6 octahedra along and around the *c* axis, respectively. The tetragonal structure assumes the $I4/mcm$ symmetry with a unit cell of $\sqrt{2}a_p \times \sqrt{2}a_p \times 2a_p$ and the same unit cell can be used to describe the antiferromagnetic structure that is also of the *G* type with the magnetic moments pointing in the direction

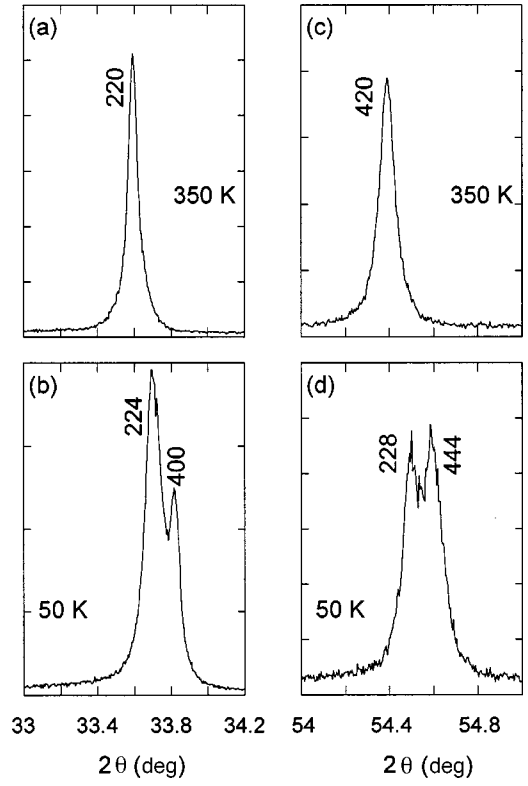

FIG. 6. Synchrotron x-ray data (for the $x=0.2$ sample) showing the tetragonal splitting of the cubic 220 (a) and 420 (c) lines into tetragonal 224 and 400 (b) and 228 and 444 (d) lines.

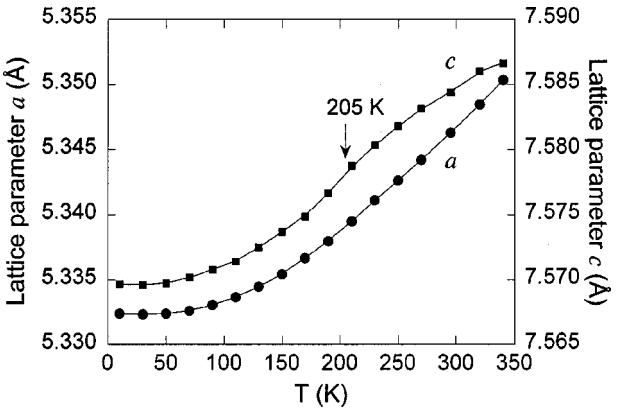

FIG. 7. Lattice parameters *a* and *c* for tetragonal $Sr_{0.7}Ca_{0.3}MnO_3$ as a function of temperature.

of the *c* axis [inset of Fig. 4(b)]. Figure 7 shows the smooth increase of the lattice parameters *a* and *c* (for $Sr_{0.7}Ca_{0.3}MnO_3$) as a function of temperature with a clear magnetostrictive response observed (in the *c* parameter) at ~205 K.

3. The orthorhombic structure

Further lowering of the symmetry from tetragonal to orthorhombic is observed as the Ca content increases for $x \geqslant 0.4$. Figure 4(c) shows the best-fit Rietveld refinement for $Sr_{0.1}Ca_{0.9}MnO_3$ using the 10 K neutron-diffraction data. The orthorhombic structure of $Sr_{1-x}Ca_xMnO_3$ can be described using the symmetry of the *Pbnm* space group in which the

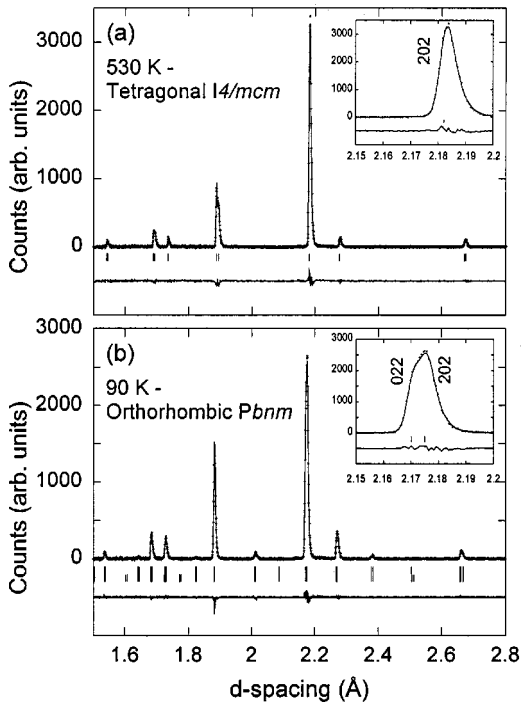

FIG. 8. Portions of best-fit Rietveld refinements for $Sr_{0.5}Ca_{0.5}MnO_3$ at 530 K (tetragonal) and at 90 K (orthorhombic). Inset shows the splitting of the tetragonal 202 line into orthorhombic 022 and 202 lines.

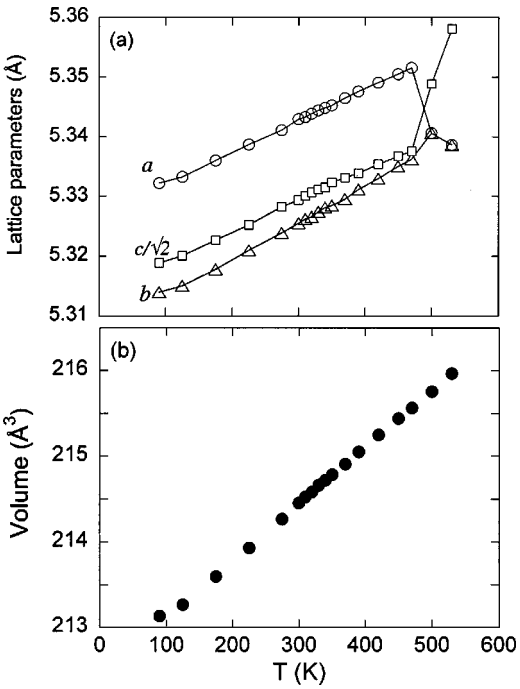

FIG. 9. (a) Lattice parameters and (b) unit-cell volume of $Sr_{0.5}Ca_{0.5}MnO_3$ as a function of temperature.

MnO_6 octahedra are rotated around and tilted off the *c* axis. The antiferromagnetic structure retains the *G*-type configuration with the magnetic moments pointing along the *c* axis [inset of Fig. 4(c)].

Figure 8(a) shows portions of best-fit Rietveld refinements using neutron-diffraction data for $Sr_{0.5}Ca_{0.5}MnO_3$ at 530 K and at 90 K demonstrating the tetragonal-to-orthorhombic structural transition. Below the transition temperature $T \sim 500$ K, the figure shows extra reflections at ~2.01 and 2.39 Å together with the splitting of the tetragonal 202 line (at ~ 2.2 Å) into two orthorhombic 202 and 022 lines. Plotting the refined lattice parameters of $Sr_{0.5}Ca_{0.5}MnO_3$ as a function of temperature shows the splitting of the tetragonal *a* parameter (becoming *a* and *b* in the orthorhombic structure) and a steep decrease in the magnitude of the *c* axis, Fig. 9(a). No abrupt changes were seen in the unit-cell volume that decrease smoothly as a function of decreasing temperature, Fig. 9(b). Similar behavior of the lattice parameters was seen for the $Sr_{0.6}Ca_{0.4}MnO_3$ sample below 280 K.

Evolution of the room-temperature unit-cell volume, T_N, and the average Mn-O-Mn bond angle is plotted as a function of $\langle r_A \rangle$ in Figs. 10(a) and 10(b), respectively. The figure shows the expected increase of the volume as a function of increased average ionic size of the *A* site and a scaling between T_N and the average Mn-O-Mn bond angle for $x \geqslant 0.3$ giving evidence for a direct link between the two parameters in the noncubic region. In the cubic regime ($x = 0 - 0.2$ and $y \leqslant 0.2$) where the Mn-O-Mn bond angle is straight, the lattice size continues to expand with decreasing Ca content and then increasing Ba content ($\langle r_A \rangle$ increasing continuously) while T_N initially increases and then decreases, respectively. This unusual behavior clearly indicates that the average Mn-

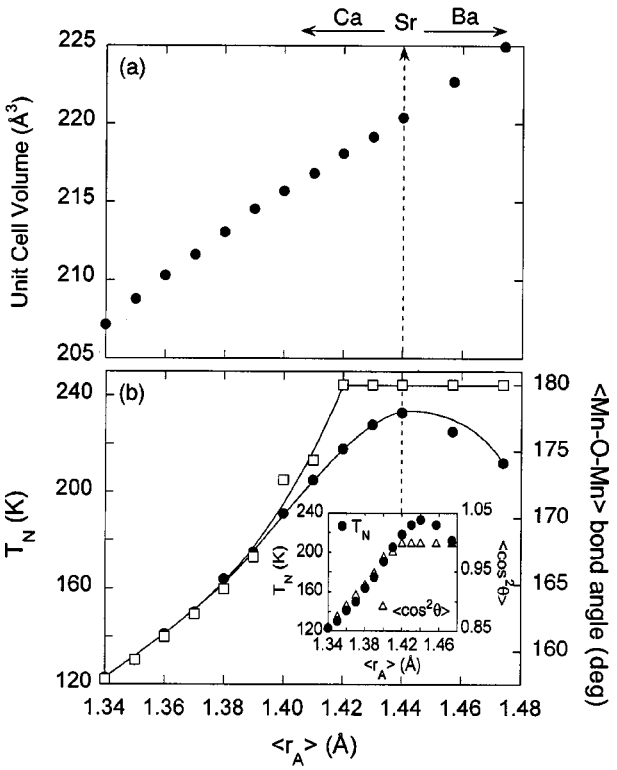

FIG. 10. (a) The room temperature unit-cell volume for $Sr_{1-x}Ca_xMnO_3$ ($0 \leqslant x \leqslant 1$) and $Sr_{1-y}Ba_yMnO_3$ ($y \leqslant 0.2$). (b) T_N (filled circles) and ⟨Mn-O-Mn⟩ bond angle (θ) (open squares) as a function of $\langle r_A \rangle$. The inset shows T_N and $\langle \cos^2 \theta \rangle$ (open triangles) plotted as a function of $\langle r_A \rangle$.

O-Mn bond angle is not the only parameter affecting T_N. Similarly, the behavior of T_N over the whole cubic region cannot be explained by the increase of the unit-cell size.

As mentioned in the Introduction, T_N and

$$\langle \cos^2 \theta \rangle [= \{\cos^2(B\text{-O1-}B) + 2\cos^2(B\text{-O2-}B)\}/3]$$

were determined to be linearly related in orthorhombic rare-earth orthoferrites and manganese-based materials.[9–12] While this relationship works reasonably well for our orthorhombic and tetragonal samples, inset of Fig. 10(b), with an average Mn-O-Mn bond angle of less than 180° it cannot account for the observed variation of T_N in the cubic regime. Rodriguez-Martinez and Attfield[13] and Attfield, Kharlanov, and McAllister[14] analyzed the relationship between T_C and the average A site ionic size for a large number of samples that belong to the colossal magnetoresistance $AMnO_3$ materials[13] and the superconducting A_2CuO_4 series[14] and proposed an empirical relation between T_C and $(r_A^0 - \langle r_A \rangle)^2$ and σ^2 that can be written as

$$T_m(\langle r_A \rangle, \sigma^2) = T_m(r_A^0, 0) - p_1(r_A^0 - \langle r_A \rangle)^2 - p_2\sigma^2, \quad (1)$$

where $\langle r_A \rangle$ is the average A-site cation radius, r_A^0 is the ideal A-site radius for an undistorted cubic perovskite, σ^2 is the variance of the A-site cation radius distribution (defined in the Introduction), $T_m(\langle r_A \rangle, \sigma^2)$ is the observed magnetic transition temperature, and $T_m(r_A^0, 0)$ is the ideal temperature of magnetic transition, p_1 and p_2 are constants. It should be noted that σ^2 is zero when there is no variance at the A site as in the case of $CaMnO_3$ and $SrMnO_3$, while $(r_A^0 - \langle r_A \rangle)^2$ is zero when the average ionic radius $\langle r_A \rangle$ equals that of an ideal cubic perovskite r_A^0. In our case this is achieved when the system becomes cubic near the $x = 0.2$ composition and as such r_A^0 in our system is ~1.42 Å at room temperature.

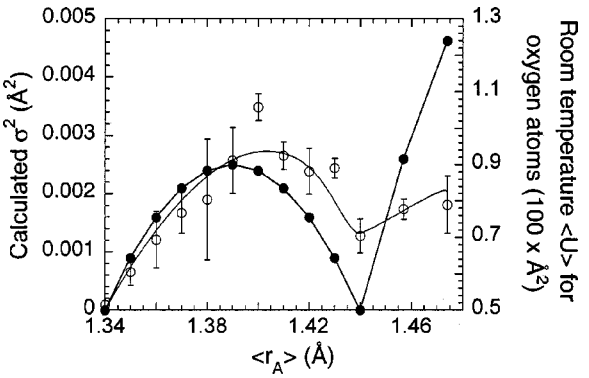

FIG. 11. Calculated σ^2 (filled circles) and the measured room temperature Debye-Waller factor $\langle U \rangle$ (open circles) for the oxygen atoms as a function of $\langle r_A \rangle$.

Using geometrical arguments, the linear relationship between $(r_A^0 - \langle r_A \rangle)^2$ and $\langle \cos^2 \theta \rangle$ can be easily verified. Thus, we prefer to use the well-established parameter $\langle \cos^2 \theta \rangle$ for describing the behavior of T_N.[9–12] Similarly, the variance of the Mn-O-Mn bond angle from its average value can be approximated by the parameter σ^2. It should be stressed that the A-site cation mixing causes local variations of the Mn-O-Mn bond angle even when the average angle is 180°. In theory, these distortions can be deduced from the Debye-Waller factors of the oxygen atoms measured at low temperatures and as such the two parameters would be linearly related as shown by Rodriguez-Martinez and Attfield.[31] In practice, however, the low-temperature Debye-Waller factors remain contaminated by contributions from thermal effects, thus, making it difficult to extract meaningful or accurate values for the variation of the local angular distortions. In Fig. 11 we plot the calculated σ^2 and the average Debye-Waller factor for oxygen atoms measured at room temperature as a function of $\langle r_A \rangle$ showing the similarity in the be-

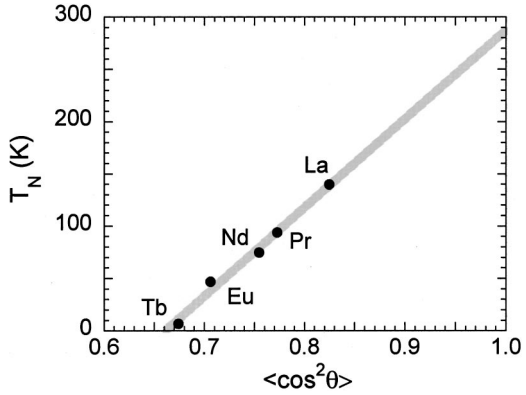

FIG. 12. T_N vs $\langle \cos^2 \theta \rangle$ for $REMnO_3$ (RE=La, Pr, Nd, Eu, and Tb) materials with $\sigma^2 = 0$. Data extracted from Refs. 32–36.

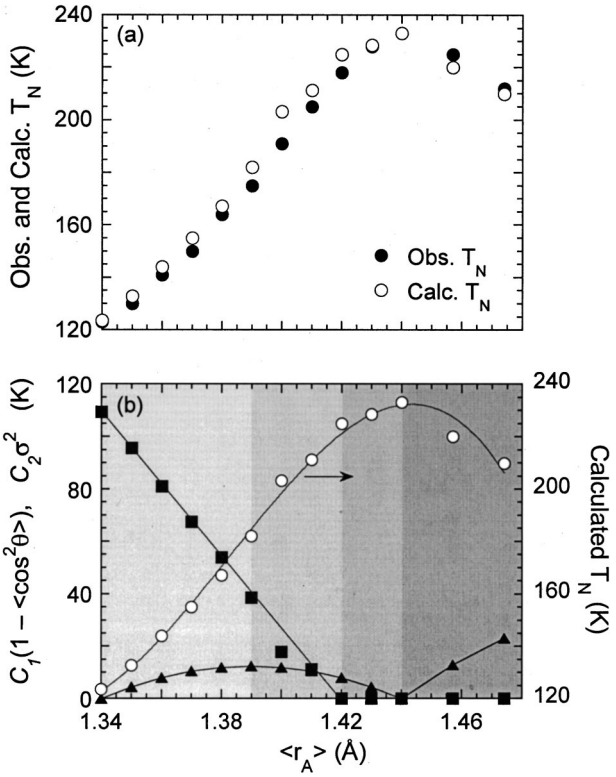

FIG. 13. (a) Observed (filled circles) and calculated T_N (open circles) as a function of $\langle r_A\rangle$. (b) Calculated T_N values (open circles) obtained by subtracting the individual contributions of $C_1(1-\langle\cos^2\theta\rangle)$ (filled squares) and $C_2\sigma^2$ (filled triangles) from $T_{N_{\max}}$ of 233 K [see Eq. (2) in the text].

havior of the two parameters. Thus, taking $[\cos^2(180°)-\langle\cos^2\theta\rangle]$ and σ^2 as parameters affecting the ideal temperature of the magnetic transition, Eq. (1) can be written as

$$T_N(\theta,\sigma^2)=T_{N_{\max}}(180°,0)-C_1(1-\langle\cos^2\theta\rangle)-C_2\sigma^2, \quad (2)$$

where C_1 and C_2 are the variation rates of T_N as a function of $\langle\cos^2\theta\rangle$ and σ^2, namely, $dT_N/d(\langle\cos^2\theta\rangle)$ and $dT_N/d\sigma^2$, respectively. In this equation, σ^2, $\langle\cos^2\theta\rangle$, and $T_{N_{\max}}(180°,0)=233$ K are known and C_1 and C_2 can be independently determined. In the cubic region of $Sr_{1-x}Ca_xMnO_3(x\leqslant 0.2)$ and $Sr_{1-y}Ba_yMnO_3(y\leqslant 0.2)$, where $(1-\langle\cos^2\theta\rangle)$ is null, we determined the ratio $dT_N/d\sigma^2$ as $C_2\sim 5000(500)$ K/Å^2. The parameter C_1 was determined from a plot depicting T_N vs $\langle\cos^2\theta\rangle$ that we constructed for $\sigma^2=0-REMnO_3$ materials [RE (rare earth) is La, Pr, Nd, Eu, and Tb], in Fig. 12, using T_N and $\langle\cos^2\theta\rangle$ values from Refs. 32–36. The figure shows a linear relation between T_N and $\langle\cos^2\theta\rangle$ from which we calculate the $dT_N/d(\cos^2\theta)$ratio$=C_1$ as $\sim$770(70) K. This value is comparable to a C_1 of $\sim$520(50) K that can be extracted from the T_N vs $\langle\cos^2\theta\rangle$ plot shown in Ref. 10 for the rare-earth orthoferrites. It is worth mentioning that the extrapolated value of $T_{N_{\max}}(180°,0)$ is $\sim$285(10) K for an ideal cubic $AMn^{3+}O_3$ perovskite (Fig. 12) against a value of $\sim$810 K for the $REFeO_3$ materials.[10]

As shown in Fig. 13(a), T_N values calculated using Eq. (2) are in good agreement with the observed T_N values over the whole range of $\langle r_A\rangle$ regardless of the structural symmetry of the perovskite material. Structural parameters used in these calculations are listed at the bottom of Table I.

Figure 13(b) shows T_N values calculated using Eq. (2) together with the individual contributions of σ^2 and $(1-\langle\cos^2\theta\rangle)$ as a function of $\langle r_A\rangle$. To emphasize these individual contributions, we divide the figure into four shaded areas as shown. The linear curve (filled squares) represents the variation of $C_1(1-\langle\cos^2\theta\rangle)$, the inverse parabola (filled triangles) represents the calculated *A*-site variance $C_2\sigma^2$, and the open circles show the variation of T_N as a function of $\langle r_A\rangle$. In the first area, the negative impact of σ^2 (increasing away from its first minimum at $CaMnO_3$) on T_N is overcompensated by the positive effect of $(1-\langle\cos^2\theta\rangle)$ on T_N decreasing rapidly towards its minimum. In the second part, σ^2 reverses sign and decreases towards its second minimum at $SrMnO_3$ and the two parameters collaborate positively to keep T_N increasing faster. At the onset of the third area, $(1-\langle\cos^2\theta\rangle)$ reaches its zero value and remains as such throughout the cubic region, thus, having no effect on T_N in this region. The variance σ^2, on the other hand, continues to decrease towards its second minimum (at $SrMnO_3$) and keeps T_N increasing but at a slower rate. Finally, in the fourth part of the graph, σ^2 departs from its second minimum and decreases T_N.

IV. CONCLUSIONS

We synthesized a series of high-quality metastable $Sr_{1-x}Ca_xMnO_3(0\leqslant x\leqslant 1)$ and $Sr_{1-y}Ba_yMnO_3(y\leqslant 0.2)$ samples for the study of the dependence of the antiferromagnetic transition temperature on structural features. Magnetic, resistive, and neutron-diffraction measurements determined T_N for all samples. Neutron and synchrotron x-ray diffraction experiments showed that the nuclear structure changes from cubic to tetragonal to orthorhombic as a function of decreased average size of the *A*-site cation similar to other transition-metal perovskites. Our data show a reasonable scaling between T_N and $\langle\cos^2\theta\rangle$ in the orthorhombic and tetragonal regimes. In the cubic regime, however, we observe a continuous change in T_N for a constant Mn-O-Mn bond angle (i.e., constant $\langle\cos^2\theta\rangle$). Similarly, the parabolic behavior of T_N cannot be explained by the monotonic increase of the unit-cell size. These observations demonstrate a need for consideration of the local variations of the Mn-O-Mn bond angles that are related to the *A*-site size variance σ^2. We show that optimal $T_{N\,\max}$ is suppressed by two contributions $C_1(1-\langle\cos^2\theta\rangle)$ and $C_2\sigma^2$ where C_1 and C_2 equal 770(70) K and 5000(500) K/Å^2, respectively.

ACKNOWLEDGMENTS

We wish to thank Simine Short for her help with neutron-diffraction data collection. Work at NIU was supported by the ARPA/ONR and by the State of Illinois under HECA. At ANL, this work was also supported by the U.S. Department of Energy—Office of Science under Contract No. W-31-109-ENG-38.

[1] A. Urushibara, Y. Moritomo, T. Arima, A. Asamitsu, G. Kido, and Y. Tokura, Phys. Rev. B **51**, 14 103 (1995).
[2] P. Schiffer, A. P. Ramirez, W. Bao, and S.-W. Cheong, Phys. Rev. Lett. **75**, 3336 (1995).
[3] H. Y. Hwang, S.-W. Cheong, P. G. Radaelli, M. Marezio, and B. Batlogg, Phys. Rev. Lett. **75**, 914 (1995).
[4] K. Kikuchi, H. Chiba, M. Kikuchi, and Y. Syono, J. Solid State Chem. **146**, 1 (1999).
[5] M. Hervieu, C. Martin, A. Maignan, G. Van Tendeloo, Z. Jirak, J. Hejtmanek, A. Barnabe, D. Thopart, and B. Raveau, Chem. Mater. **12**, 1456 (2000).
[6] S. Kolesnik, B. Dabrowski, O. Chmaissem, Z. Bukowski, and J. Mais, J. Appl. Phys. **89**, 7407 (2001).
[7] J. B. MacChesney, H. J. Williams, J. F. Potter, and R. C. Sherwood, Phys. Rev. **164**, 779 (1967).
[8] J. B. Goodenough, Phys. Rev. **164**, 785 (1967).
[9] D. Treves, M. Eibschütz, and P. Coppens, Phys. Lett. **18**, 216 (1965).
[10] C. Boekema, F. Van Der Woude, and G. A. Sawatzky, Int. J. Magn. **3**, 341 (1972).
[11] J. L. Garcia-Munoz, J. Fontcuberta, M. Suaaidi, and X. Obrados, J. Phys.: Condens. Matter **8**, L787 (1996).
[12] K. Asai, K. Fujiyoshi, N. Nishimori, Y. Satoh, Y. Kobayashi, and M. Mizoguchi, J. Phys. Soc. Jpn. **67**, 4218 (1998).
[13] L. M. Rodriguez-Martinez and J. P. Attfield, Phys. Rev. B **54**, R15 622 (1996).
[14] J. P. Attfield, A. L. Kharlanov, and J. A. McAllister, Nature (London) **394**, 157 (1998).
[15] R. D. Shannon, Acta Crystallogr., Sect. A: Cryst. Phys., Diffr., Theor. Gen. Crystallogr. **A32**, 751 (1976).
[16] T. Negas and R. S. Roth, J. Solid State Chem. **1**, 409 (1970).
[17] K. R. Poeppelmeier, M. E. Leonowicz, J. C. Scanlon, J. M. Longo, and W. B. Yelon, J. Solid State Chem. **45**, 71 (1982).
[18] Z. Zeng, M. Greenblatt, and M. Croft, Phys. Rev. B **59**, 8784 (1999).
[19] J. Briatico, B. Alascio, R. Allub, A. Buttera, A. Caneiro, M. T. Causa, and M. Tovar, Phys. Rev. B **53**, 14 020 (1996).
[20] G. H. Jonker, Physica (Amsterdam) **22**, 707 (1956).
[21] D. G. Hinks, B. Dabrowski, J. D. Jorgensen, A. W. Mitchell, D. R. Richards, and D.-L. Shi, Nature (London) **333**, 836 (1988).
[22] B. Dabrowski *et al.* (unpublished).
[23] J. D. Jorgensen, J. J. Faber, J. M. Carpenter, R. K. Crawford, J. R. Haumann, R. L. Hitterman, R. Kleb, G. E. Ostrowski, F. J. Rotella, and T. G. Worton, J. Appl. Crystallogr. **22**, 321 (1989).
[24] A. C. Larson and R. B. von Dreele, General Structure Analysis System, University of California, 1985–1990.
[25] W. N. Shafarman, D. W. Koon, and T. G. Castner, Phys. Rev. B **40**, 1216 (1989).
[26] N. F. Mott, J. Non-Cryst. Solids **1**, 1 (1969).
[27] J. J. Neumeier and J. L. Cohn, Phys. Rev. B **61**, 14 319 (2000).
[28] C. J. Ball, B. D. Begg, D. J. Cookson, G. J. Thorogood, and E. R. Vance, J. Solid State Chem. **139**, 238 (1998).
[29] S. Qin, A. I. Becerro, F. Seifert, J. Gotsmann, and J. Jiang, J. Mater. Chem. **10**, 1609 (2000).
[30] J. Garcia-Jaca, J. L. Mesa, M. Insausti, J. I. R. Larramendi, M. I. Arriortua, and T. Rojo, Mater. Res. Bull. **34**, 289 (1999).
[31] L. M. Rodriguez-Martinez and J. P. Attfield, Phys. Rev. B **58**, 2426 (1998).
[32] J. A. Alonso, M. J. Martinez-Lope, M. T. Casais, and M. T. Fernandez-Diaz, Inorg. Chem. **39**, 917 (2000).
[33] Z. Jirák, J. Hejtmánek, E. Pollert, M. Marysko, M. Dlouhá, and S. Vratislav, J. Appl. Phys. **81**, 5790 (1997).
[34] I. O. Troyanchuck, N. V. Samsonenko, N. V. Kasper, H. Szymczak, and A. Nabialek, J. Phys.: Condens. Matter **9**, 8287 (1997).
[35] M. Mukovskii, G. Hilscher, H. Michor, and A. M. Ionov, J. Appl. Phys. **83**, 7163 (1998).
[36] J. Blasco, C. Ritter, J. Garía, J. M. de Teresa, J. Pérez-Cacho, and M. Ibarra, Phys. Rev. B **62**, 5609 (2000).